PROCEEDINGS, 41st Workshop on Geothermal Reservoir Engineering
Stanford University, Stanford, California, February 22-24, 2016
SGP-TR-209

Revisiting Stimulation Mechanism at Fenton Hill and an Investigation of the Influence of Fault Heterogeneity on the Gutenberg-Richter b-value for Rate-and-State Earthquake Simulations

Jack H. Norbeck[1], Mark W. McClure[2], and Roland N. Horne[1]

[1]Department of Energy Resources Engineering, Stanford University, Stanford, California, 94025, USA

[2]McClure Geomechanics LLC, Palo Alto, California, 94301, USA

jnorbeck@stanford.edu

Keywords: induced seismicity, fault heterogeneity, rate-and-state friction, poroelasticity, earthquake modeling

ABSTRACT

In this work, we developed a numerical modeling framework for application to subsurface reservoir engineering problems related to fluid flow, heat transfer, and mechanical deformation in fractured porous media. An existing reservoir simulator was extended to include poroelastic and thermoelastic effects. We introduced a novel approach to couple poroelastic and thermoelastic stresses with fracture deformation calculations. In addition, we implemented a rate-and-state friction model capable of describing the earthquake rupture process on two-dimensional heterogeneous fault surfaces. A spatial random field model was used to generate heterogeneous, spatially correlated, fractal distributions of fault properties such as stress, friction, and permeability.

We applied the numerical model to investigate reservoir stimulation efforts at the Fenton Hill enhanced geothermal system test site. A geologic conceptual model of the site was developed based on several independent datasets. Several scenarios were simulated to isolate the roles of fluid pressurization of the fractures, poroelastic stress, and thermal stress. Comparing the simulation results with the actual earthquake catalog data indicates that poroelastic and thermoelastic effects likely did play a role during the Fenton Hill stimulation treatments. Our analysis also suggests that shear stimulation did not contribute to enhanced permeability at the Fenton Hill reservoir.

In another study, we hypothesized that by introducing heterogeneous and spatially correlated patterns of fault properties, it would be possible to simulate earthquake sequences that exhibit power law scaling of frequency-magnitude distributions using a rate-and-state friction model. We examined the influence of heterogeneous distributions of initial shear stress, initial normal stress, dynamic friction coefficient, and permeability. Our model was able to simulate earthquake sequences exhibiting Gutenberg-Richter-type frequency-magnitude distributions with b-values close to 1 when the fault had heterogeneous stress or friction. Permeability heterogeneity did not have an effect. This study has implications for understanding how the Gutenberg-Richter b-value is influenced by natural geologic conditions and injection well operations.

1. INTRODUCTION

Apart from ground motion estimates, the most influential parameters in earthquake hazard analysis are the seismicity rate, recurrence rate of a given-magnitude earthquake, and the Gutenberg-Richter (GR) b-value (Petersen et al., 2015). If these earthquake statistics can be quantified accurately, then the data can be combined to develop a probabilistic estimate of earthquake hazard for a particular area. In a recent study, van der Elst (2015) found that the maximum magnitude earthquake events observed in 21 separate cases of injection-induced seismicity were each as large as expected statistically based on the local earthquake catalogs. Characterization of the hydromechanical reservoir response to fluid injection must therefore be cast in terms of understanding how these types of earthquake statistics can be expected to change due to injection operations.

Numerical reservoir models are useful tools for investigating how natural geologic and injection conditions can affect seismicity, but it can often be difficult to generate realistic earthquake sequences using physics-based seismicity models. In this work, we developed a reservoir model that couples unsteady-state flow, heat transfer, and mechanical deformation in fractured porous media. The modeling framework is flexible enough to consider many different types of geologic conditions and operational settings. In this work, we performed two separate numerical experiments related to injection-induced seismicity. We first investigated how different physical processes can influence the evolution of seismicity during relatively short hydraulic stimulation treatments of naturally fractured geothermal reservoirs. The goal was to determine whether porothermoelastic effects played a role at the Fenton Hill enhanced geothermal system (EGS) test site. Next, we modeled sequences of induced earthquakes along a large basement fault. The purpose of this study was to determine how fault heterogeneity can affect the frequency-magnitude distribution of simulated earthquake events.

The remainder of this paper is organized as follows. In Section 2, we present the numerical formulation for the reservoir model used in this work. The fluid flow, heat transfer, and geomechanics model components are each described. In addition, the rate-and-state friction formulation for two-dimensional faults and a model used to generate fractal distributions of fault properties are described. In Section 3, we present the results from an investigation of induced seismicity at the Fenton Hill EGS site. In Section 4, we present the results from a synthetic study of injection-induced seismicity in a wastewater disposal setting. We modeled sequences of injection induced earthquakes along basement faults with heterogeneous, spatially correlated stress, friction, and permeability. The GR b-value was characterized for each case. In Section 5, we discuss the implications of this research and present several concluding remarks.

2. FRACTURED AND FAULTED RESERVOIR MODELING FRAMEWORK

In this section, we present the numerical formulation for each physical process considered in the model: fluid flow, heat transfer, fracture mechanics, and porothermoelasticity. The boundary element approach used to solve for fracture deformation and fracture propagation is described in detail in McClure and Horne (2013) and McClure et al. (2016). Here, we describe a three-dimensional treatment for earthquake rupture within a rate-and-state friction framework. In addition, we describe a method to incorporate heterogeneity in stress, frictional properties, and hydraulic properties along fracture and fault surfaces into the model.

We used different numerical discretization techniques for the various components of the model. For both the fluid flow and heat transfer components, an embedded fracture modeling approach was used to couple mass and heat transfer between the faults, fractures, and surrounding rock. Embedded fracture is an extension of a traditional finite volume method. The fracture and fault mechanics component was based upon the displacement discontinuity method, which is a type of a boundary element method. The displacement discontinuity method is accurate for calculating mechanical deformation in large networks of interacting faults and fractures. Because the matrix of Green's functions relating changes in stress to displacement discontinuities along the fracture surfaces is fully dense in the general case, we employed an algorithm described by Bradley (2014) to perform the matrix-vector-products involved in the stress updates efficiently. Although quasistatic elasticity problems are governed by an elliptic differential equation, the rock displacements can evolve in time due to the coupling with fluid flow and heat transfer. The model included both implicit Euler and explicit Runge-Kutta methods to advance the solution through time, depending on the nature of the problem being solved. Finally, a finite element method was used in the porothermoelastic component. The approach described in Section 2.3.4 for coupling induced stresses with fracture deformation is particularly convenient within our embedded fracture modeling framework, because the finite element shape functions provide the ability to resolve spatially varying poroelastic- or thermoelastic-induced tractions back onto fracture surfaces.

2.1 Fluid Flow

We considered a fractured and porous medium saturated with a single phase fluid. In the embedded fracture approach, it is useful to consider the fractured (faulted) volume and the intact matrix rock volume as separate, but coupled, computational domains. For flow in the matrix domain, mass conservation can be expressed as:

$$\nabla \cdot \left(\rho_\varphi \lambda k^m \nabla p^m \right) + \tilde{m}^{wm} + \tilde{\Psi}^{fm} = \frac{\partial}{\partial t} \left(\rho_\varphi \phi^m \right). \tag{1}$$

For flow in the matrix domain, mass conservation is:

$$\nabla \cdot \left(\rho_\varphi \lambda e k^f \nabla p^f \right) + \tilde{m}^{wf} + \tilde{\Psi}^{mf} = \frac{\partial}{\partial t} \left(\rho_\varphi E \right). \tag{2}$$

All variables, subscripts, and superscripts in this paper are defined in the Nomenclature section. Mass transfer between the two domains occurs through the coupling terms, $\tilde{\Psi}$, which depend predominantly on the fracture-matrix surface area (Norbeck et al., 2015). For rock and fluid properties typical of geothermal reservoirs, Eq. 1 is often only slightly nonlinear due to the relatively low compressibility of the pore fluid and matrix rock, but Eq. 2 can be highly nonlinear because the hydraulic and void aperture of fractures and faults can be affected significantly by changes in fluid pressure, mechanical opening, and shear dilation. Equations 1 and 2 were discretized using a finite volume strategy.

2.2 Heat Transfer

Fluid is assumed to be in thermal equilibrium with the reservoir rock. Energy conservation can be expressed as:

$$\nabla \cdot \left(\kappa^m \nabla T^m \right) - \nabla \left[\rho_\varphi c_\varphi \mathbf{v}^m \left(T^m - T_0^m \right) \right] + c_\varphi \tilde{m}^{wm} \left(T^w - T_0^m \right) + \tilde{\Pi}^{fm} = \frac{\partial}{\partial t} \left\{ \left[\phi^m \rho_\varphi c_\varphi + \left(1 - \phi^m \right) \rho_r c_r \right] \left(T^m - T_0^m \right) \right\}, \tag{3}$$

and:

$$\nabla \cdot \left(\kappa^f \nabla T^f \right) - \nabla \left[\rho_\varphi c_\varphi \mathbf{v}^f \left(T^f - T_0^f \right) \right] + c_\varphi \tilde{m}^{wf} \left(T^w - T_0^f \right) + \tilde{\Pi}^{mf} = \frac{\partial}{\partial t} \left\{ \left[\phi^f \rho_\varphi c_\varphi + \left(1 - \phi^f \right) \rho_r c_r \right] \left(T^f - T_0^f \right) \right\}. \tag{4}$$

The heat transfer equations have a similar form to the mass balance equations, except that additional advection terms appear to account for the heat that is transported with the fluid. The fluid velocity was calculated using Darcy's law:

$$\mathbf{v} = -k \lambda \nabla p \ . \tag{5}$$

A traditional upwinding scheme was used when evaluating the advection terms. Thermal conductivity was calculated as a volumetric average of the solid rock and fluid constituents as $\kappa = \phi \kappa_\varphi + (1 - \phi \kappa_r)$. When modeling heat transfer, one may distinguish between fractures that act essentially as open voids (i.e., $\phi^f = 1$) and faults that act as a porous media (i.e., $\phi^f \neq 1$) by noting that the effective porosity is related to the void aperture, E ,and the physical width, W ,of the feature as $\phi^f = E / W$.

The embedded fracture coupling terms for the heat transfer equations have a similar form as in Eqs. 1 and 2, but now contain an additional term related to advection of heat between the two domains:

$$\Pi^{mf} = \omega\left(T^{m} - T^{f}\right) + c_{\varphi}\Psi^{mf}\left(T - T_{0}\right). \tag{6}$$

Upwinding must be used when evaluating the advection term. In this work, we used an iterative sequential strategy to couple fluid flow and heat transfer.

2.3 Geomechanics and Earthquake Rupture Model

For a porous rock volume subjected to a change in pressure from a reference state, Δp, Hooke's law for isotropic material properties is:

$$\boldsymbol{\sigma}^{P} = 2G\boldsymbol{\varepsilon} + \Lambda\,\mathrm{trace}\left(\boldsymbol{\varepsilon}\right) + \alpha\Delta p\mathbf{I}. \tag{7}$$

Analogously, for rock subjected to a change in temperature from a reference state, ΔT, Hooke's law is:

$$\boldsymbol{\sigma}^{T} = 2G\boldsymbol{\varepsilon} + \Lambda\,\mathrm{trace}\left(\boldsymbol{\varepsilon}\right) + 3\beta K\Delta T\mathbf{I}. \tag{8}$$

It is important to recognize that $\boldsymbol{\sigma}^{P}$ and $\boldsymbol{\sigma}^{T}$ are the changes in total stress that are generated if the material is constrained in some way from deformation. Assuming infinitesimal strains and using Eqs. 7 and 8 as constitutive relationships between stress and strain, conservation of momentum can be expressed as:

$$G\nabla^{2}\mathbf{u} + \left(\Lambda + G\right)\nabla\left(\nabla\cdot\mathbf{u}\right) = -\mathbf{f} - \alpha\nabla\left(\Delta p\right) - 3\beta\nabla\left(\Delta T\right). \tag{9}$$

In this work, we routinely took advantage of the fact that superposition of displacements and stresses holds for a linear elastic material. For example, the state of stress at a particular location in the material reflects the superposition of the remote tectonic stress, $\boldsymbol{\sigma}^{R}$, mechanically-induced stress caused by fracture deformation, $\boldsymbol{\sigma}^{M}$, and porothermoelastic effects:

$$\boldsymbol{\sigma} = \boldsymbol{\sigma}^{R} + \boldsymbol{\sigma}^{M} + \boldsymbol{\sigma}^{P} + \boldsymbol{\sigma}^{T}. \tag{10}$$

We are free to solve Eq. 9 in separate steps and superimpose their effects, so long as the boundary conditions are upheld appropriately. We solved the thermoelastic and poroelastic deformation problem using a finite element approach based on the fluid pressure and temperature distributions obtained from the solution of Eqs. 1 – 4. Then, we resolved $\boldsymbol{\sigma}^{P}$ and $\boldsymbol{\sigma}^{T}$ onto any existing fracture surfaces and added their effect to other tractions acting as boundary conditions for the fracture deformation problem, which was solved using a boundary element method. The field displacements caused by fracture deformation only influence the porothermoelastic problem indirectly through changes in matrix porosity that can induce flow. In this work, we neglected changes in matrix porosity caused by changes in total stress.

2.3.1 Equilibrium Equations for Fracture and Fault Deformation

In order to solve the fracture (fault) deformation problem, we enforced mechanical equilibrium along the fracture surfaces. Throughout a simulation, the state of stress at each discretized fracture element was checked and updated continuously. We assumed that fractures bearing compressive effective normal stress can be considered mechanically closed (may still be open to fluid flow) and should deform in the mode-I (opening) direction subject to a nonlinear joint stiffness constitutive law. In the model, closed fracture elements did not add any degrees of freedom to the global problem, and their mode-I deformations were updated explicitly. If the effective normal stress acting on a fracture element is reduced to zero, the fracture should deform subject to fracture mechanics theory. The mode-I mechanical equilibrium equation for open fractures is:

$$\overline{\sigma}_{n} = \sigma_{n}^{R} + \sigma_{n}^{M} + \sigma_{n}^{P} + \sigma_{n}^{T} - p^{f} \equiv 0. \tag{11}$$

The term on the left hand side is the effective normal stress, which reflects the combined effects of fracture deformation-induced stress, poroelastic stress, thermal stress, and fluid pressure acting within the fracture. Equations 1, 2, and 11 were solved simultaneously in a fully implicit nonlinear framework for p^{f}, p^{m}, and the mode-I displacement discontinuity, δ_{n}.

To solve the mode-II (sliding) deformation problem, we assumed a Mohr-Coulomb shear failure criterion. The frictional strength of a fracture, $\overline{\tau}$, is defined as:

$$\overline{\tau} = f\overline{\sigma}_{n} + S. \tag{12}$$

A model assumption is that if the shear stress acting on a fracture is less than its frictional resistance to slip (i.e., $\tau < \overline{\tau}$), then mode-II deformations can be neglected. Otherwise, mode-II mechanical equilibrium for closed fractures is:

$$\tau = \tau^R + \tau^R + \tau^R + \tau^R + \tau^R - \eta V \equiv f\overline{\sigma}_n + S \,, \tag{13}$$

and for open fractures is:

$$\tau \equiv 0 \,. \tag{14}$$

For a two-dimensional fracture plane, τ is the magnitude of the shear traction vector (i.e., $\tau = \sqrt{\sigma_s^2 + \sigma_d^2}$). The direction of sliding is calculated as $\theta = \tan^{-1}(V_d / V_s)$. The sliding velocity, V , is the time rate of change of the mode-II displacement discontinuities, δ_s ,and δ_d , resolved in the direction of sliding:

$$V = \sqrt{V_s^2 + V_d^2} = \sqrt{\left(\frac{\partial \delta_s}{\partial t}\right)^2 + \left(\frac{\partial \delta_d}{\partial t}\right)^2} \,. \tag{15}$$

We applied different approaches for solving the mode-II deformation problem. If the coefficient of friction was assumed constant or if a static/dynamic friction approach was used, Eqs. 13 and 14 were solved using an implicit Euler scheme. In that case, an iterative sequential approach was used to couple sliding with the flow and mode-I deformation solutions. For rate-and-state friction problems, we used an explicit Runge-Kutta method. In that case, a single sequential step coupled sliding to the flow and mode-I deformation solutions.

2.3.2 Rate-and-state Friction

Rate-and-state friction is useful for modeling sequences of earthquakes repeated along the same fault because it allows for friction restrengthening. It has also been shown to provide solutions to the earthquake rupture problem that are convergent upon discretization refinement. In a rate-and-state framework, friction depends on V and also on a state variable, Θ , that accounts for the history of sliding. Two common regularizations for the coefficient of friction are (Rice et al., 2001):

$$f(V,\Theta) = a \sinh^{-1}\left[\frac{V}{2V_*}\exp\left(\frac{\Theta}{a}\right)\right] , \tag{16}$$

and

$$f(V,\Theta) = a \ln\frac{V}{V_*} + \Theta \,. \tag{17}$$

Equation 16 is more suitable for numerical computations as $V \to 0$. The rate-and-state a parameter controls the magnitude of the direct effect, which causes an immediate strengthening for increasing V . During the coseismic period of an earthquake rupture, the state variable controls the friction weakening behavior along the fault behind the rupture front. As a rupture dies out, the state variable increases to bring the fault back to equilibrium. Two forms of state evolution have been proposed that are each able to describe different sets of laboratory friction experiments. The slip law allows state to evolve only when the fault is sliding (Rice et al., 2001):

$$\frac{\partial \Theta}{\partial t} = -\frac{V}{L}\left[f(V,\Theta) - f_{ss}(V)\right] . \tag{18}$$

The aging law can be expressed as (Rojas et al., 2009):

$$\frac{\partial \Theta}{\partial t} = -\frac{V}{L}\left\{b - b\exp\left[-\frac{f(V,\Theta) - f_{ss}(V)}{b}\right]\right\} . \tag{19}$$

The two state evolution laws have different physical implications, so we have incorporated both forms of state evolution into the model to allow for further testing.

The particular forms chosen to represent friction and state evolution in Eqs. 16 – 19 have several interesting advantages both in terms of physical interpretation and numerical behavior. State is represented as a dimensionless variable, and has a magnitude on the order of the friction coefficient. Therefore, it is more stable numerically than when represented with units of time (e.g., see McClure and Horne, 2011), where it can change over many orders of magnitude very rapidly. In addition, the state evolution equations are able to consider any functional form for the steady-state friction coefficient. Recent laboratory experiments have shown that friction can undergo extreme weakening at very high slip speeds approaching $V_{\max} \approx 1$ m/s. This can have a significant impact, for example, on interpreting earthquake rupture behavior on faults with low normal stress like the San Andreas Fault (Dunham et al., 2011). In this work, we used a more traditional form for steady-state friction:

$$f_{ss}(V) = f_* - (b - a)\ln\frac{V}{V_*}. \quad (20)$$

Effective normal stress can also be very low in settings of injection-induced seismicity, so investigating how alternate forms of f_{ss} affect the earthquake rupture process may be a worthwhile pursuit in future research.

2.3.3 Heterogeneous, Spatially Correlated, Fractal Distributions of Stress, Fault Friction, and Hydraulic Aperture

In the three-dimensional version of the present model, fractures and faults are represented as two-dimensional surfaces and discretized into rectangular elements. Each of the rate-and-state parameters (a, b, L, f_*, V_*) can be heterogeneous over the fault surface. Hydraulic and void aperture (e and E) can also be considered heterogeneous fault properties. Finally, one of the most important aspects of this model is its ability to handle spatially and temporally variable stress states while enforcing mechanical equilibrium rigorously, so it is clear that stress can also be considered a heterogeneous fault property.

The significance of heterogeneous properties in terms of understanding the hydromechanical behavior of fractures and faults have been highlighted in many previous theoretical, laboratory, and field studies. Andrews (1980) argued that stress heterogeneity over a range of spatial scales contributed to the power law form of the commonly observed Gutenberg-Richter-type frequency-magnitude distribution of earthquake events. Okubo and Aki (1987) measured the roughness of the trace of the San Andreas Fault, and observed that it could be described as a fractal pattern. Ishibashi et al. (2015) performed laboratory flow experiments on samples of granitic rocks in order to investigate how fracture surface roughness affected fluid flow for joints and sheared fractures at several different confining pressures and over several different length scales. In that study, it was observed that the heterogeneous fracture aperture distribution caused flow channeling to occur, and it was suggested that these effects could have significant impacts in terms of mass transport or heat transfer. Moreover, both the fracture aperture distributions and the effective fracture surface area were found to be scale-invariant (fractal). Mai and Beroza (2002) analyzed coseismic slip distributions of real earthquakes using finite source models, and found that the slip patterns could be well characterized by a fractal decay model.

In this work, we applied a spatial random field model to generate heterogeneous, spatially correlated distributions of fault properties. For a two-dimensional fault plane, the power spectral density, $P(\kappa_s, \kappa_d)$, is a function of the spatial wave numbers in the strike and slip directions, κ_s and κ_d, and follows a power law decay that is related to the fractal dimension, D:

$$P(\kappa_s, \kappa_d) \propto \frac{1}{\left(\kappa_s^2 + \kappa_d^2\right)^{4-D}}. \quad (21)$$

For application to earthquake rupture numerical models, the practical range of wave number depends on the size of the model fault and the size of a discretized fault element. Equation 21 was used to define P over the practical wave number range and fractal dimension of interest, random phase angles were applied to perturb P in the Fourier domain to create a unique pattern, and then P was inverted into the real space domain, as described by Voss (1988). Higher values of D yielded a more random, less spatially correlated pattern. For example, filtering the same random field at several different values of D yielded the distributions shown in Fig. 1.

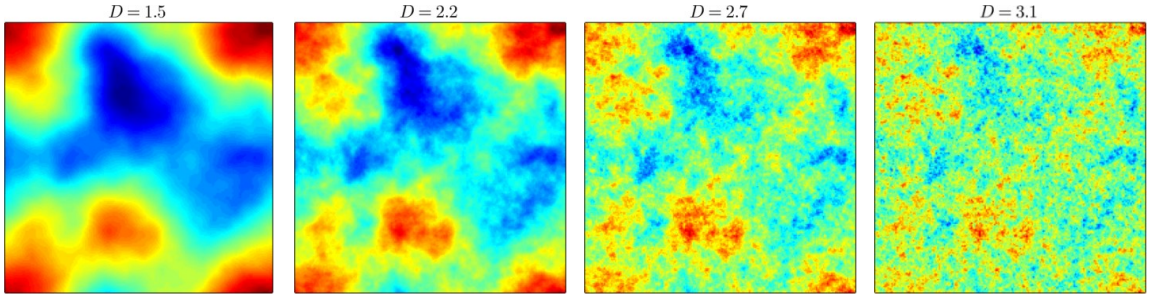

Figure 1: Example illustrations of one realization of a random field model for four different values of fractal dimension. The range of spatial correlation is reduced for higher fractal dimension.

2.3.4 Poroelasticity and Thermoelasticity

The porothermoelastic model of Norbeck and Horne (2015, 2016) was extended by implementing the finite element formulation described by Smith, Griffiths, and Margetts (2014). The model can handle both two-dimensional plane strain rectangular elements (4 node, 8 node, and 9 node quadrilateral) and general three-dimensional cuboidal elements (8 node, 14 node, and 20 node hexahedra). Upon discretization with the finite element method, Eq. 9 is reduced to a linear system of equations involving the displacement vectors at the finite element nodes:

$$\mathbf{k}\,\mathbf{u} = \mathbf{f}. \quad (22)$$

For an unconstrained material, Eq. 7 can be inverted to calculate the strains that would occur due to a change in fluid pressure. In the plane strain case, for example, the poroelastic strains are:

$$\boldsymbol{\varepsilon}^P = \begin{Bmatrix} \varepsilon_{xx} \\ \varepsilon_{yy} \\ 2\varepsilon_{xy} \end{Bmatrix}^P = -\frac{\alpha}{3K}\Delta p^m \begin{Bmatrix} 1 \\ 1 \\ 0 \end{Bmatrix}. \tag{23}$$

The equivalent nodal forces that would cause those strains to occur are:

$$\mathbf{f} = \iint \mathbf{B}^T \mathbf{D}\, \boldsymbol{\varepsilon}^P \, dxdy \quad . \tag{24}$$

In Eq. 24, $\mathbf{B}$ is a matrix of partial derivatives relating nodal displacements to strain within the finite element and $\mathbf{D}$ is the Hooke's law matrix relating stress to strains.

A significant issue to deal with here is that, in our proposed modeling framework, a finite volume grid is used for the flow problem where the fluid pressures are calculated as cell-centered values and represent the average pressure over each control volume. If we use, for example, a conventional four node quadrilateral finite element for the poroelastic problem, the fluid pressure is assumed to be continuous at the finite element nodes at the corners of each element. One possible approach could be to use staggered grids so that the finite element nodes coincide with the finite volume cell centers. In this work, we chose instead to use the same grids for the finite element and finite volume discretizations. Bilinear interpolation was performed to map the fluid pressure distribution to approximate values at the finite element nodes. Then, Eq. 24 was evaluated for each finite element using numerical integration.

Equation 22 was assembled into a global system of equations and solved for the nodal displacement vectors. At the element level, the total strains were calculated as:

$$\boldsymbol{\varepsilon} = \mathbf{B}\mathbf{u} \quad . \tag{25}$$

The $\mathbf{B}$ matrix relates displacements at the finite element nodes to strain within the element, and is therefore a function of location within the element. In our application to fractured reservoir problems, we evaluated $\mathbf{B}$ at each discrete fracture element. Finally, we used Hooke's law to calculate the poroelastic stress change:

$$\boldsymbol{\sigma}^P = \mathbf{D}\left(\boldsymbol{\varepsilon} - \boldsymbol{\varepsilon}^P\right). \tag{26}$$

In this way, we were able to approximate nonuniform distributions of induced stress along fracture surfaces even if there were many fracture elements contained in a single grid block, which we have found to be the usual case in practical applications of our embedded fracture model. Thermal stresses were calculated in exactly the same manner. In this case, the thermal strains were used to calculate the equivalent nodal force vector:

$$\boldsymbol{\varepsilon}^T = \begin{Bmatrix} \varepsilon_{xx} \\ \varepsilon_{yy} \\ 2\varepsilon_{xy} \end{Bmatrix}^T = -\beta\Delta T^m \begin{Bmatrix} 1 \\ 1 \\ 0 \end{Bmatrix}. \tag{27}$$

3. INVESTIGATION OF INDUCED SEISMICITY DURING RESERVOIR STIMULATION EXPERIMENTS AT THE FENTON HILL EGS TEST SITE

This work was performed as part of an ongoing collaborative effort led by the U.S. Department of Energy (DOE) Geothermal Technologies Office (White et al., 2015). The overarching goal of the DOE-led geothermal code comparison project is to learn more about how the characteristics of the fractured reservoir system influenced the reservoir stimulation process Fenton Hill Enhanced Geothermal System (EGS) test site. At the time of the Fenton Hill project, two competing hypotheses of the hydraulic stimulation mechanism were held by the scientists and engineers involved in the project (Brown et al., 2009). One camp believed that planar hydraulic fractures were forming in the reservoir, while the other camp believed that stimulation was attributed to deformation of preexisting fractures and no hydraulic fractures were forming. An advantage of working as part of the DOE code comparison team is that we are able to leverage diverse backgrounds to help analyze and interpret complex, interdisciplinary datasets that were generated during the Fenton Hill EGS project to develop improved conceptual models.

In the present study, we were interested in understanding how fracture pressurization, poroelastic stress, and thermal stress affected the evolution of microseismicity that was observed during various injection experiments carried out during the 1980's. We focused on four stimulation treatments in well EE-2 leading up to and including the massive hydraulic fracture (MHF) experiment (Expts. 2018, 2020, MHF Pre-pump, and Expt. 2032). The DOE provided microseismic event locations and timing recorded during Expt. 2032 (MHF). In Fig. 2, the event locations are shown in plan and cross-section views and are color-coded by timing. During injection, events migrated away from the well. In plan view, the microseismic cloud tended to migrate in an overall NNW-SSE direction. This is an extremely important observation, and helps to form the basis for our reservoir conceptual model. Figure 3a shows the radial distance away from

the well of each event over time. The solid lines represent radial pressure diffusion profiles assuming different (constant) hydraulic diffusivities. The data cannot be represented by a single diffusion profile, suggesting that the diffusivity may have been nonlinear. During injection, events tended to occur across the entire stimulated region. Upon shut-in after 2.5 days of injection, the events occurred predominantly at the edges of the stimulated region, and the events migrated back towards the well. In Fig. 3b, the event rate overlies the injection pressure during the MHF experiment. At early times, no events were recorded which was likely due to the Kaiser effect as a result of previous injection experiments. During injection at constant flow rate, the pressure was observed to be relatively constant, however, the seismicity rate could be characterized by several distinct rate spikes. Following shut-in, the event rate decayed steadily over the period of about 1 day.

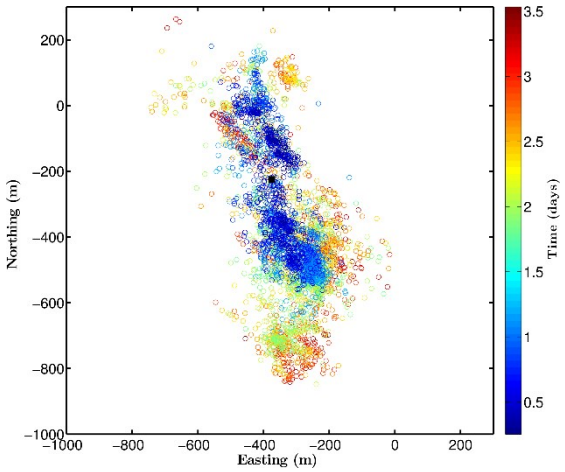

Figure 2: Microearthquake locations recorded during the Expt. 2032 (MHF) stimulation treatment at Fenton Hill colored by event timing. The well was shut-in after roughly 2.5 days.

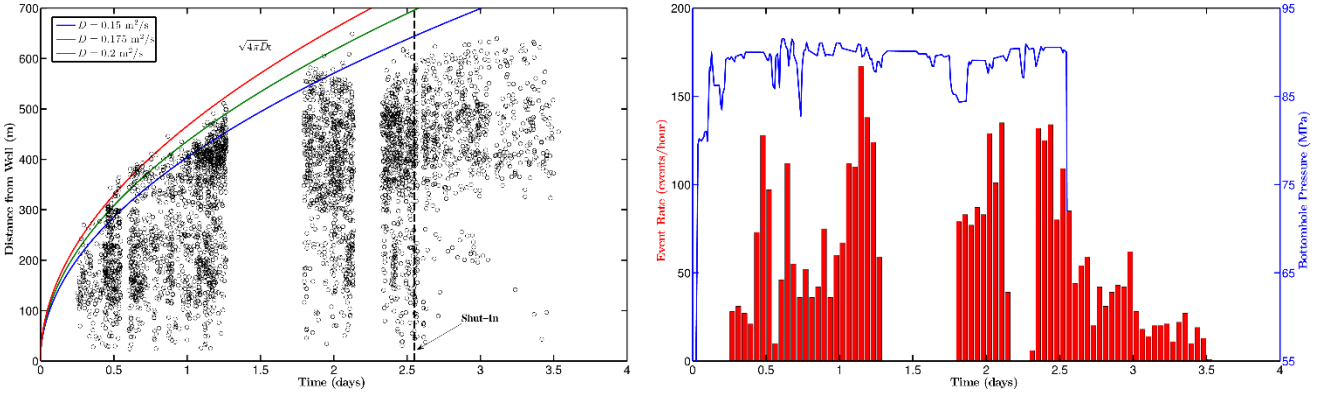

(a) **(b)**

Figure 3: (a) Distance from the well location for each event in the catalog and (b) event rate and bottomhole pressure during Expt. 2032 (MHF) at Fenton Hill. The earthquake catalog and well operational data were provided by Los Alamos National Laboratory and Pacific Northwest National Laboratory as part of the DOE geothermal code comparison study.

3.1 Conceptual and Numerical Model Descriptions

The injection experiments took place in well EE-2, which had an openhole interval at a depth of roughly 3.6 km in the Phase II reservoir at Fenton Hill. Our interpretation for the state of stress in the Phase II reservoir is based off of wellbore stress measurements (Barton and Zoback, 1988), earthquake focal mechanisms (House et al., 1985), minifrac tests (Kelkar et al., 1986; Brown, 1989), and observations during step-rate tests (Brown et al., 2012). Varying estimates of the fracture gradient are available in the literature. Kelkar et al. (1986) summarized a large number of minifrac tests to estimate that the minimum principal stress gradient was 19 MPa/km, implying a value of 68.4 MPa at 3.6 km depth. However, Kelkar et al. (1986) noted that tests shallower than 3.3 km depth indicated a much lower fracture gradient. Based on these and other observations, Brown (1989) proposed that the minimum principal stress gradient was 13 MPa/km, implying a stress of 46.8 MPa. Brown (1989) hypothesized that due to the high strength of granite, hydraulic fractures were unable to form at the wellbore, and so the fracturing pressure observed during injection tests corresponded to the pressure required to exceed the normal stress on preexisting fractures intersecting the well. If these fractures are not perpendicular to the minimum principal stress, then their opening pressure will be greater than the minimum principal stress. Therefore, Brown (1989) proposed that the apparent increase fracturing pressure at 3.3 km was caused by a discontinuity in natural fracture orientation, rather than stress, and that the tests shallower than 3.3 km reflected the true value of the minimum principal stress.

In our model, we have chosen to use the Brown (1989) estimate for the magnitude of the minimum principal stress. In the injection tests in EE-2, the well injectivity was observed to increase very sharply and nonlinearly at a bottomhole pressure of around 74 MPa (at 3.6 km depth), and so for either stress profile, the bottomhole pressure exceeded the minimum principal stress during the injections (Figures 6-5, 6-9, 6-18, and 6-21 from Brown et al., 2012).

We assumed a strike-slip stress regime where the state of stress at depth was $\sigma_H^R \approx \sigma_V^R = 90$ MPa, $\sigma_h^R = 46$ MPa, and $p_0 = 31$ MPa. The orientation of σ_H^R was N30°E based on interpretations of wellbore breakouts (Barton and Zoback, 1988). The fractures had a constant coefficient of friction of $f = 0.7$ (rate-and-state friction was not used in the Fenton Hill study). The host rock was assumed to have a very low permeability of $k^m = 1 \times 10^{-19}$ m^2 (0.1 nd) and a porosity of $\phi^m = 0.05$. The initial reservoir temperature at the injection interval was $T_0 = 230$ °C. Elastic properties of the matrix rock were assumed to be typical of granite (Jaeger et al., 2007).

Microseismic events observed during hydraulic fracturing treatments are often interpreted as shear slip events on natural fractures that surround the main hydraulic fracture. At Fenton Hill, if this was the appropriate mechanism, then the microseismic cloud would be expected to migrate in the direction of maximum horizontal stress (N30°E), but this was not the case. Nonetheless, injection pressures during the hydraulic stimulations typically exceeded the magnitude least horizontal stress significantly (see Fig. 3b), which would suggest that hydraulic fractures were indeed forming in the reservoir. In addition, a consistent observation during multiple step-rate tests was that near wellbore injectivity increased substantially after exceeding a pressure corresponding to a bottomhole pressure of about 74 MPa (Brown et al., 2012). A conventional minifrac analysis would interpret this value at the fracture opening or fracture propagation pressure. Finally, a key observation was that wellbore temperature logs indicated three or four distinct feedzones during Expt. 2018, suggesting that natural fractures (not hydraulic fractures) were taking flow in the near wellbore region and that flow is localized into a small number of highly permeable pathways with vertical separation on the order of 100 ft (Figure 6-6 from Brown et al., 2012).

We developed a conceptual model for the Fenton Hill Phase II reservoir that is generally consistent with each of these observations. The reservoir was considered to be naturally fractured with a primary set of near-vertical fractures oriented with an average strike of NNW-SSE. Hydraulic fractures propagated as splays off the tips of the natural fractures. The hydraulic fractures do not form into large, continuous features because they sometimes terminate against natural fractures due to mechanical interference. This conceptual model is the "mixed-mechanism stimulation" concept that has been applied in oil and gas settings (Weng et al., 2011). McClure (2012) and McClure and Horne (2014) argued that this is the dominant mechanism of stimulation in many (but not all) EGS projects.

The orientation of the primary fracture set was determined based on three independent datasets that each support one another. First, the "fracture opening pressure" of 74 MPa was interpreted as the fluid pressure required to overcome the normal stress acting on natural fractures intersecting the well. Based on the state of stress, the fracture orientation corresponding to $\sigma_n^R = 74$ MPa is roughly N23°W. Second, analysis of the focal mechanisms for several of the largest observed microearthquakes yielded solutions with a nodal plane suggesting the presence of fracture or fault structures oriented N30°W (House et al., 1985). Finally, the overall migration of the seismicity was in the NNW-SSE direction. We generated a stochastic realization of a fractured reservoir based on this conceptual model for the simulations performed in this study. The reservoir model and Mohr circle representation of the stress state is shown in Fig. 4.

The hydraulic fractures need to be present in the model for several reasons. First, the fluid pressure exceeds the minimum principal stress, and so it is plausible that hydraulic fractures would form. Even if the high tensile strength of the rock prevents hydraulic fractures from forming at the well, concentrations of stress created by natural fracture opening and sliding natural will facilitate the formation of hydraulic fractures away from the well. Because the fluid pressure increases well-above the minimum principal stress, the hydraulic fractures can mechanically open to large apertures and provide the bulk of the fluid storage during injection. However, it is critical for the hydraulic fractures to terminate against the natural fractures, because otherwise, they would propagate continuously across the formation, and the microseismic cloud would orient primarily perpendicular to the minimum principal stress, which was not actually observed. In the simulations, fracture termination was assumed to occur 50% of the time when a hydraulic fracture reached a natural fracture.

We performed four simulations in order to isolate the effects of different physical processes that could have potentially contributed to the seismicity observed during the stimulation treatments. We investigated the relative impact of fluid pressurization in the fractures, poroelastic stress, and thermal stress (Cases A, B, and C, respectively) and also performed one simulation that incorporated all of the mechanisms (Case D). Fluid pressurization is the most common mechanism associated with injection-induced seismicity. Poroelastic stresses can be generated as fluid pressure in the rock surrounding the fractures changes due to leakoff or production. Thermal stresses can be generated as the rock is cooled during injection. The full schedule of injection, production, and shut-in history over the course of roughly 17 months was simulated. Important model parameters provided in Table A-1 of Appendix A.

In Fig. 6, we compare the event distance and event rate over time for Cases A-D. The models were able to capture several important characteristics observed in the real data. In each case, the lag in the onset of seismicity caused by the Kaiser effect was captured. As new natural fractures were connected to the well sporadically through hydraulic fracturing, bursts in seismicity occurred. The maximum event distance increases during injection similar to Fig. 3a. For each case, the maximum event distance did not increase following shut-in. A significant difference in post shut-in behavior was observed between Case A (pressure only) and the other three cases. For Case A, the post shut-in events occurred much closer to the well than in Cases B-D. In the actual catalog data, the events tended to occur far from the well at the edges of the stimulated region. Our results suggest that poroelastic and thermal effects likely contributed to the seismicity at Fenton Hill, because these effects encouraged post shut-in events to occur further from the well.

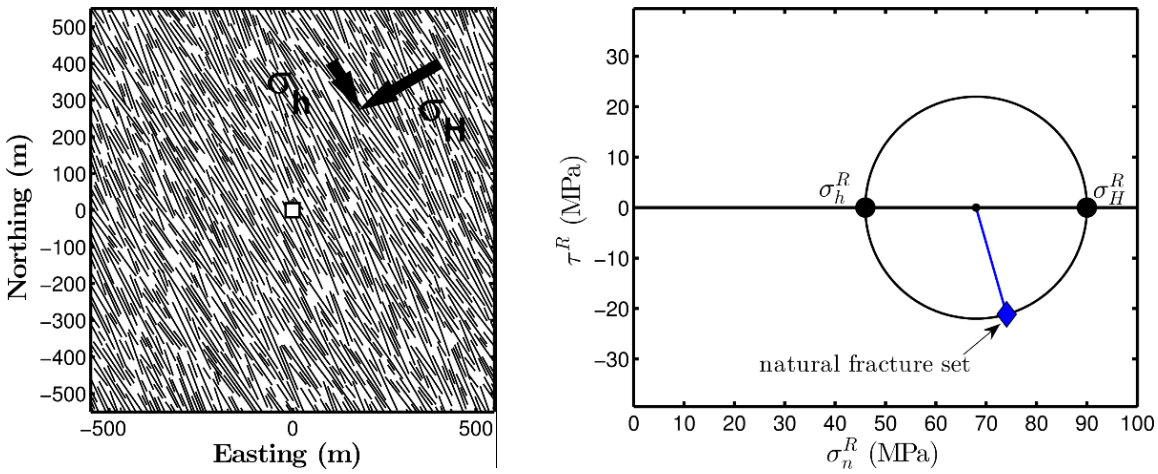

(a) **(b)**

Figure 4: (a) Fractured reservoir model used in the simulations and (b) the stress state for the Fenton Hill Phase II reservoir. A primary set of natural fractures is oriented with an average strike of N23°W. Stimulation occurs through a mixed-mechanism combination of natural fracture mechanical opening and propagation of hydraulic splay fractures.

Each of the different physical processes had a significant impact on the migration of seismicity. In Case A, the events migrated away from the wellbore uniformly. When poroelastic stress was introduced in Case B, the events migrated predominantly in the North direction. In Case C, the thermal stresses evidently encouraged the growth of the stimulated region compared to Case A. The effect of poroelastic and thermoelastic stresses on the seismicity is best interpreted from analysis of the change in Coulomb stress:

$$\Delta\sigma_C = |\Delta\tau| - f\Delta\bar{\sigma}_n \,. \tag{28}$$

A positive $\Delta\sigma_C$ indicates that the new state of stress has improved the likelihood of shear failure. The pressure and temperature distributions at the end of the MHF for Case D are shown in Figs. 7a and 7b, respectively. We resolved the poroelastic and thermal stresses into normal and shear components on the natural fractures, and used Eq. 28 to calculate the change in Coulomb stress (shown in Figs. 7c and 7d, respectively). In these numerical experiments, the poroelastic and thermal stress changes were on the order of 1 MPa. The change in fluid pressure in the fractures was on the order of 10-50 MPa, clearly dominating the overall effective stress. Nonetheless, the stimulation treatments were very sensitive to the presence of the additional physical mechanisms. The combined change in Coulomb stress at the end of Expts. 2020 and 2032 are shown in Fig. 8. The microseismic events that occurred during each of the stimulation treatments are shown as black dots. Although the magnitude of the change in Coulomb stress is small compared to the change in fluid pressure within the fractures, areas of the reservoir that experienced a decreased Coulomb stress tended to have fewer microseismic events.

Finally, we must remark on a critical observation during the injection experiments on well EE-2 at Fenton Hill. In the first stimulation (Expt. 2018), the well had extremely low injectivity until reaching a critical pressure threshold, upon which further increases in injection rate resulted in relatively low changes in injection pressure. According to Brown et al. (2012), this same behavior was observed in the subsequent three stimulation treatments (Expts. 2020, MHF prepump, and 2032), with a remarkably consistent critical threshold of a wellhead pressure of 5500 psia (roughly 74 MPa at 3.6 km depth). We interpret this as caused by hydromechanical opening of the fractures intersecting the well. In Fig. 9, we show the simulated results for bottomhole pressure and injection rate during the four stimulation treatments. In each case, the bottomhole pressure increased dramatically at low flow rates until reaching a critical pressure threshold, similar to the actual injection data (see Fig. 3b).

We reiterate that the injectivity at low flow rates did not change even after several repeated stimulation treatments in well EE-2. In order to model this behavior, we used a shear dilation angle of zero. Therefore, the simulation results suggest that shear stimulation was not effective at enhancing the permeability of natural fractures at Fenton Hill. Our analysis suggests that stimulation occurred as a mixed-mechanism combination of mechanical fracture opening (as the fluid pressure in natural fractures approached their normal stress) and creation of hydraulic splay fractures.

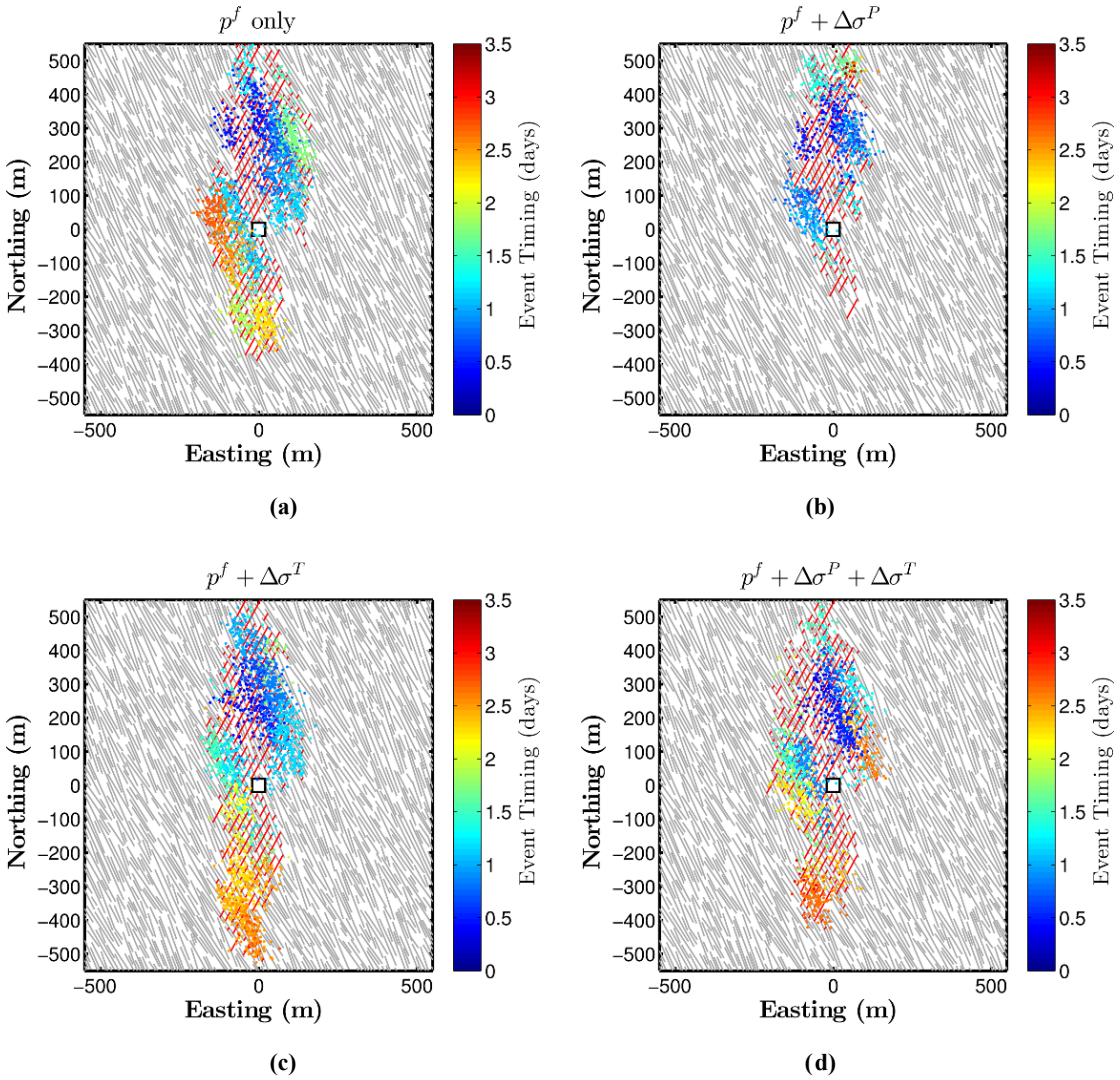

Figure 5: Stimulated fracture network and microseismic event locations at the end of Expt. 2032 (MHF) for (a) Case A, (b) Case B, (c), Case C, and (d), Case D. The red lines are hydraulic splay fractures generated during the stimulation treatment.

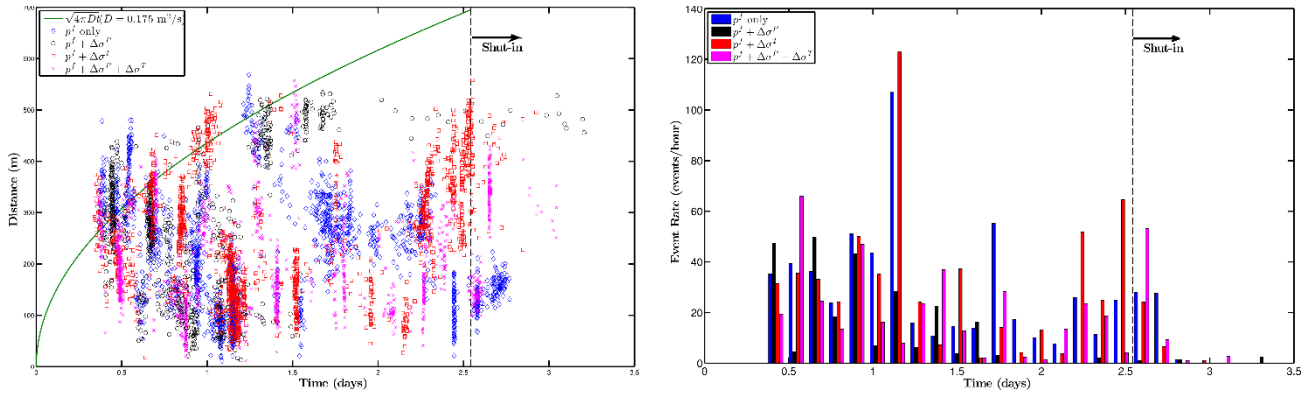

Figure 6: Comparison of (a) distance from well and (b) event rate for Cases A – D during Expt. 2032.

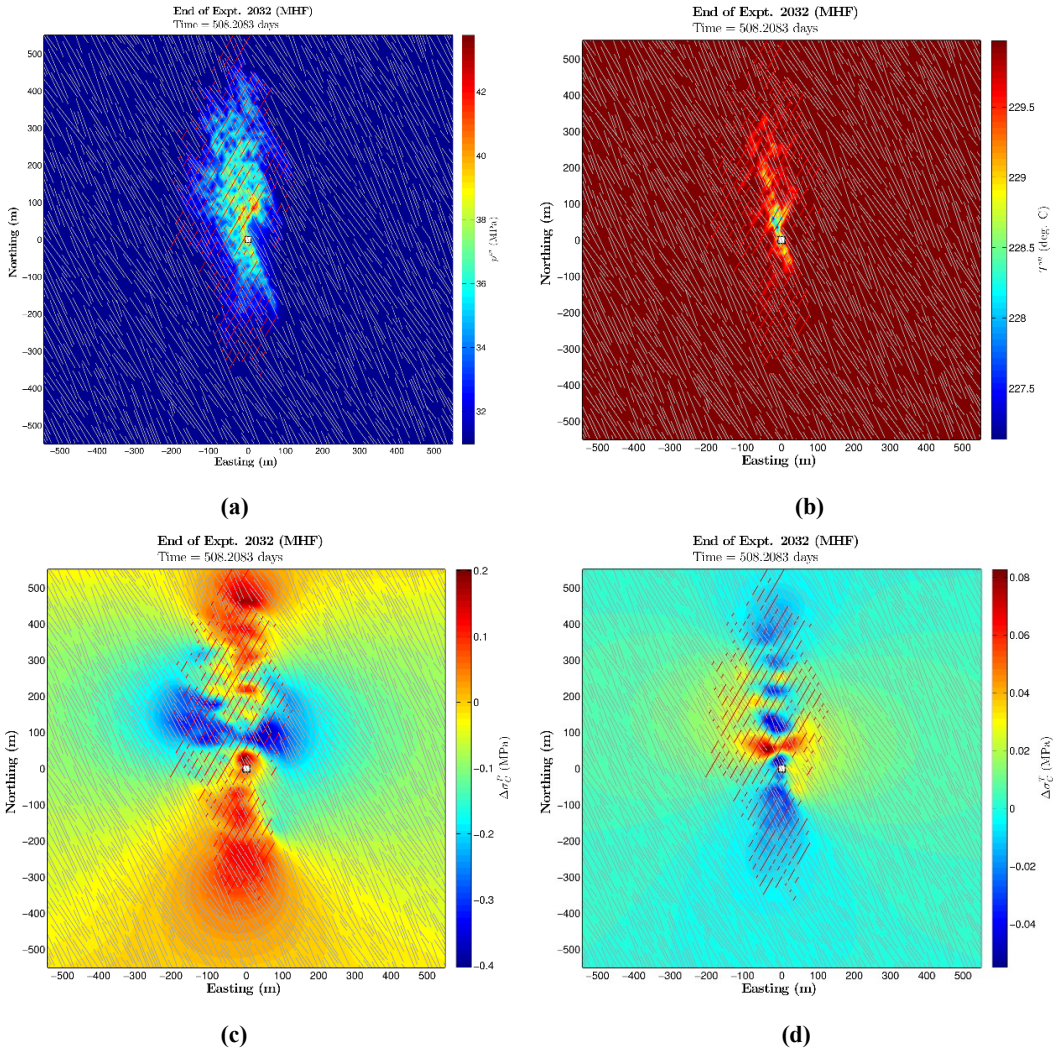

Figure 7: Distribution of (a) matrix fluid pressure, (b) matrix temperature, (c) change in Coulomb stress caused by poroelastic effects, and (d) change in Coulomb stress caused by thermal effects at the end of Expt. 2032 (MHF) for Case D.

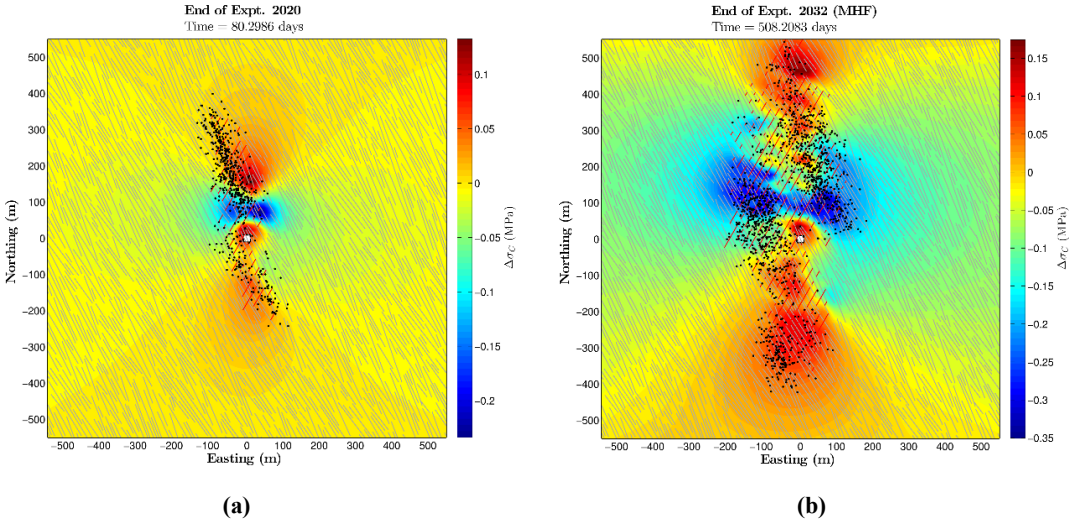

Figure 8: Contours of total change in Coulomb stress (a) at the end of Expt. 2020 and (b) at the end of Expt. 2032. The black dots represent microearthquake event locations that occurred during each of the stimulation treatments.

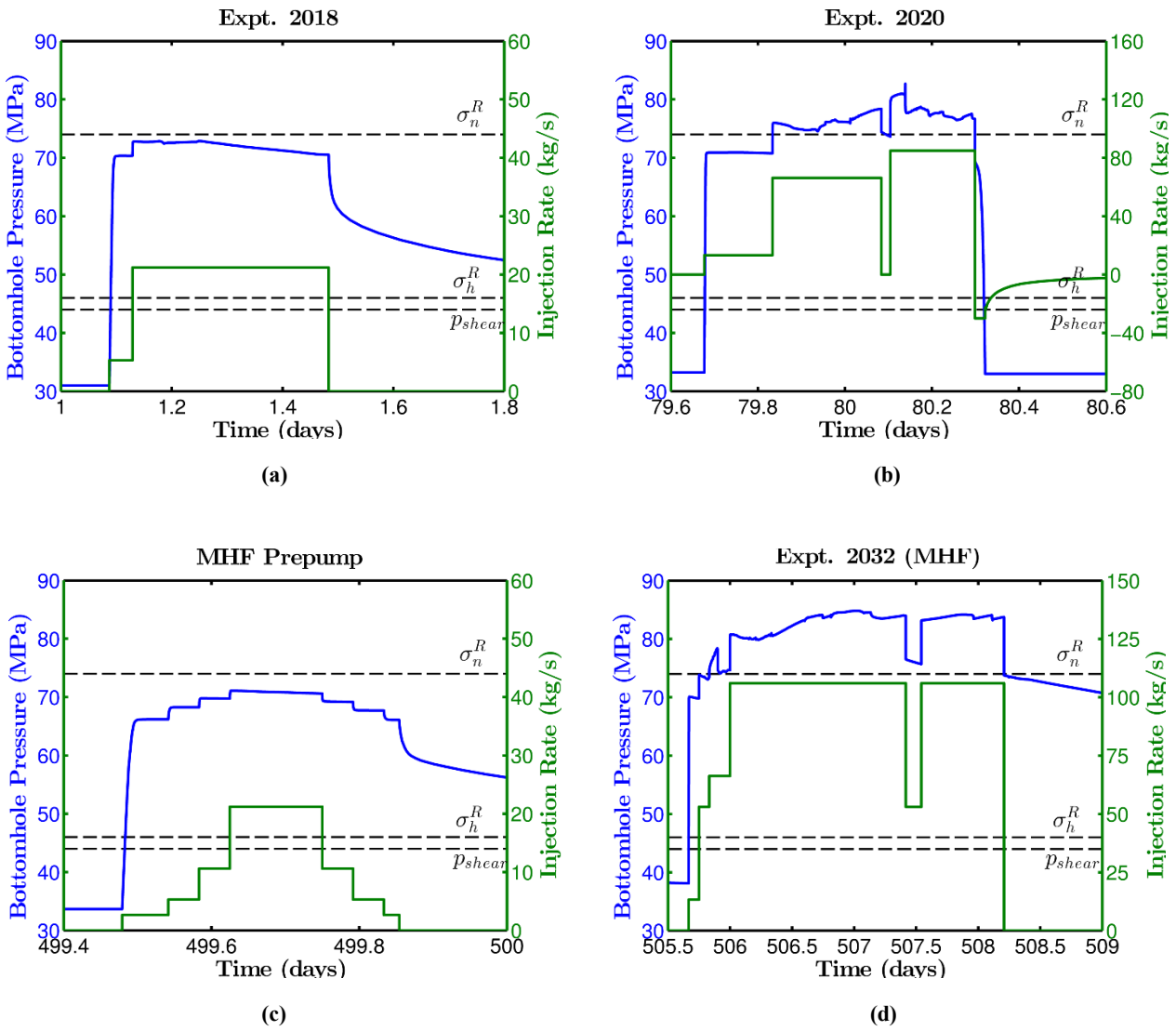

Figure 9: Bottomhole pressure and injection rate during (a) Expt. 2018 (b) Expt. 2020, (c) MHF prepump, and (d) Expt. 2032 (MHF). Consistent with the Fenton Hill injection data, the simulation results show a distinct increase in injectivity upon reaching a critical pressure threshold caused by hydromechanical fracture opening over repeated stimulation treatments.

4. PROGRESS TOWARDS UNDERSTANDING THE INFLUENCE OF FAULT HETEROGENEITY ON THE GUTENBERG-RICHTER B-VALUE FOR INJECTION-INDUCED EARTHQUAKE SEQUENCES

The Gutenberg-Richter (GR) b-value and the occurrence rate of earthquake activity are two of the most important parameters in earthquake hazard analysis (Petersen et al., 2015). If they can be quantified accurately at a particular site, then these two datasets can be combined in order to provide a probabilistic estimate of future earthquake activity. Both in natural settings and instances of injection-induced seismicity, the GR b-value has been observed to vary in space and time. Understanding how the b-value is affected by natural geologic conditions (e.g., fault friction or stress) or injection operation conditions (e.g., injection rate or shut-in events) may have important implications for hazard assessment.

Numerical modeling provides a tool to investigate how different operational strategies or site characteristics affect seismicity. Unfortunately, it is difficult to obtain GR-type frequency-magnitude distributions from earthquake rupture simulations using a rate-and-state friction framework. Modeling a single planar fault with homogeneous stress and frictional properties will tend to produce earthquake sequences with only a single event magnitude characteristic of the fault dimension (McClure and Horne, 2011; Norbeck and Horne, 2015). In reality, faults exhibit heterogeneity in many of their properties, including geometry, roughness, state of stress, and permeability. Fang and Dunham (2013) demonstrated that introducing self-similar fractal patterns of fault roughness provided a mechanism for rupture arrest to occur before the rupture front reached the edge of the fault. Dieterich et al. (2015) performed quasidynamic earthquake rupture simulations on two-dimensional fault surfaces and introduced heterogeneity in initial shear stress distributions by using either smoothed Gaussian white noise or by using the stress pattern left over from a previously simulated earthquake event. In that study, sequences of earthquakes with various event magnitudes were obtained.

In this study, we hypothesized that by introducing heterogeneous, spatially correlated fractal patterns of fault properties, power law scaling of simulated frequency-magnitude distributions could be recovered. We considered heterogeneity in initial shear stress, initial normal stress, dynamic friction coefficient, and permeability. We applied the spatial random field model described in Section 2.3.3 to generate spatially correlated fractal patterns over two-dimensional fault surfaces. For each type of fault property, we filtered the random field at four different fractal dimensions ranging from $1.5 \le D \le 3.1$, which affected the range of spatial correlation. Finally, we performed the sensitivity analysis for two different average values of the rate-and-state $(b - a)$ parameter, which affected earthquake stress drop and the ability for ruptures to propagate outside of highly pressurized zones of the fault. The high and low stress drop cases are referred to as Cases E and F, respectively. Scenarios 1 – 4 refer to the fault property being tested (1 = shear stress, 2 = normal stress, 3 = dynamic friction, 4 = permeability).

4.1 Model Description

We modeled sequences of injection-induced earthquakes along a vertical strike-slip basement fault. The fault was 4.5 km long, 1 km in vertical extent, and located at a depth of roughly 5 km. The state of stress in the model reflected central Oklahoma. We used recent measurements from central Oklahoma to constrain stress orientations and magnitudes (Rall Walsh and Mark Zoback, pers. comm.), and the fluid pressure was taken to be slightly subhydrostatic (Nelson, 2015). To introduce modest geometrical complexity, three segments of an en-echelon fault with stepover features were modeled. The strike of the fault was oriented at 40 degrees relative to the direction of maximum principal stress. Figure 10a shows a plan view of the fault geometry. Stress and fluid pressure gradients in the vertical direction were neglected.

Wastewater disposal was modeled as radial flow assuming constant rate injection into an aquifer of finite thickness (Horne, 1995). The hydraulic connection between the fault and the aquifer was modeled as a time-dependent pressure boundary condition at one of the stepover features (see the location of the red circle in Fig. 10a). The rest of the fault was surrounded by impermeable rock. The magnitude of the time-dependent pressure boundary condition was determined from the radial flow solution at a distance of 100 m from the injection well (see Fig. 10b). A ten year injection period was modeled. Important model parameters are provided in Table A-2 of Appendix A.

The fault surfaces were discretized into a total of 9020 square elements of equal side length. For the fault properties listed in Table A-2, the critical discretization length to overcome numerical convergence issues associated with resolving earthquake nucleation in the rate-and-state friction framework is $L_c \le \pi GL / [4(b - a)\bar{\sigma}_n] = 250$ m (Noda et al., 2009). The size of each grid block in our model was 25 m by 25 m.

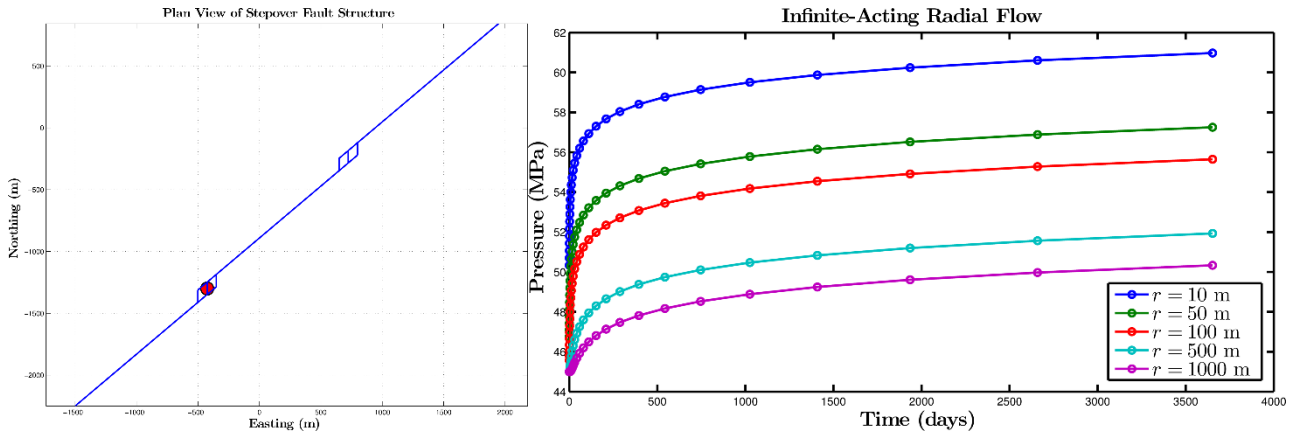

(a) **(b)**

Figure 10: (a) Plan view of the en-echelon stepover fault model geometry, and (b) infinite-acting radial flow (IARF) solution for injection into an aquifer of finite thickness and. The hydraulic connection between the well and the basement fault was assumed to occur at one of the stepover features and modeled as a time-dependent pressure boundary condition based on the IARF solution at a distance of 100 m from the well.

4.2 Sensitivity Study

We considered heterogeneous spatially correlated distributions of four different fault properties: initial shear stress, initial normal stress, dynamic friction coefficient, and permeability. For each type of property, we also investigated four different levels of spatial correlation, corresponding to fractal dimensions ranging over $1.5 \le D \le 3.1$. In each simulated scenario, the same underlying random pattern was used to generate the distribution of the property of interest. The random fields along each of the three fault segments are shown in Fig. 11.

We recognized that perturbations in shear stress, normal stress, and fault friction can each have a unique impact on the earthquake rupture process. We attempted to achieve consistency between cases involving different fault properties by controlling the magnitude of the perturbations based on their expected impact in stress drop during an individual earthquake rupture. The stress drop during an

earthquake, $\Delta\tau$, is the difference between the background initial shear stress acting on the fault well ahead of the rupture front, τ^R, and the stress level behind the rupture front during sliding, τ_D:

$$\Delta\tau = \tau^R - \tau_D \,. \tag{29}$$

We used the spatial random fields to alter the state of stress or frictional properties by adding perturbations to background (average) values of shear stress, $\delta\tau$, normal stress, $\delta\sigma$, or b in the rate-and-state friction model (which affects dynamic friction), δb. Comparing their impact on the stress drop:

$$\tau^R + \delta\tau - f_D\left(\bar{\sigma}_n^R - \delta\sigma\right) \propto \tau^R - f_D\left(\bar{\sigma}_n^R - \delta\sigma\right) \propto \tau^R - \left[f_* - (b + \delta b - a)\ln\frac{V_{\max}}{V_*}\right]\bar{\sigma}_n^R \,, \tag{30}$$

it is apparent that the following scaling relationships provide an appropriate basis for comparing the influence of random spatial fields of different fault properties:

$$\delta\tau \propto f_D\,\delta\sigma \propto \bar{\sigma}_n^R \ln\frac{V_{\max}}{V_*}\,\delta b \,. \tag{31}$$

The spatial random fields we generated had a mean value of zero and a standard deviation s. We normalized the spatial random fields such that the perturbation at one standard deviation from the mean corresponded to a perturbation of 10% of the initial shear stress (i.e., $\delta\tau^{1s} = 0.1\tau^R$).

4.3 Results

In each case with heterogeneous properties, the simulated earthquake sequences contained several hundred to several thousand individual earthquake events, so the GR b-value was able to be characterized. The frequency-magnitude distributions for Case E are shown in Fig. 12, and for Case F in Fig. 13. In each subfigure, the frequency-magnitude slope characterizing a GR b-value of 1 is represented by the black line. In general, power law frequency-magnitude distributions were observed. In most cases, the GR b-value was close to 1 over several orders of earthquake magnitude. High-magnitude earthquakes tended to be oversampled, compared to the b-value estimate over the range where a stable power law scaling was observed. Shear stress and normal stress heterogeneity appeared to affect the GR distributions most significantly, followed by frictional heterogeneity. Permeability heterogeneity was observed to have a negligible impact on altering frequency-magnitude distributions for the model parameters used in this study.

In each scenario, low-magnitude rollover was observed, which can be interpreted from either a physical or numerical perspective. In rate-and-state friction theory, earthquake nucleation is controlled by a critical stiffness that must ultimately be overcome as a coherent slipping patch grows in size. This critical length dimension scales like $L_c \propto GL/[(b-a)\bar{\sigma}_n]$. Therefore, a lower bound on earthquake magnitude, characteristic of L_c, can be expected. In this study, we increased the state evolution slip distance, L, above values typically measured in the laboratory in order to minimize discretization effects, so the magnitude at which rollover occurred in our simulations was likely overestimated relative to what might be expected to occur in real earthquake sequences.

4.3.1 Case E: Large Stress Drop

The results from the base case simulation with homogeneous fault properties are shown as black circles in Fig. 12a. In the base case, a power law trend was observed, but only over a very narrow range of event magnitude from roughly $1.5 < M < 2.2$. The trend indicates that the distribution was dominated by a cluster of three large events of roughly $M = 4.3$. In the homogeneous fault case, the spread of events at lower magnitudes can be attributed to the geometrical complexity of the fault stepover features and nonuniform pressure distribution over the fault caused by the fault's finite permeability.

In both Cases E1 and E2, $D = 1.5$ (the smoothest heterogeneity pattern) produced the most individual events. As D increased, fewer events were observed. For Case E1, different values of D did not affect the slope of the frequency-magnitude distribution significantly, but the range over which power law scaling was observed was largest for $D = 1.5$. For Case E2, the slope of the frequency-magnitude distribution was affected by D. The GR b-value was equal to 1 for $D = 3.1$, and increased to approximately 1.3 for $D = 1.5$.

Case E3 provided interesting and unexpected results. The friction heterogeneity changed the overall frequency-magnitude behavior markedly compared to the base case homogeneous fault. The total number of events was largest when $D = 2.2$, and then as the complexity of the heterogeneity continued to increase, fewer events were observed. In fact, for the scenarios when $D = 2.7$ and $D = 3.1$ fewer events were observed than for the homogeneous fault. For $D = 1.5$ and $D = 2.2$, the GR b-value was slightly higher than 1, whereas for $D = 2.7$, the GR b-value was much shallower than 1. For $D = 3.1$, a reliable GR b-value could not be interpreted.

In general, fault permeability can influence the earthquake rupture process by affecting the distribution of effective normal stress on the fault. Heterogeneous permeability fields cause areas of increased pressure drop across low permeability regions, which could influence

the rupture nucleation and arrest process. However, the two-dimensional flow regime in the fault plane coupled with the diffusive nature of pressure effectively smoothed out the pressure distribution in the simulations. For example, Fig. 14 shows the pressure distribution along the fault for Case E4 with $D = 2.7$ after 422 days of injection. Even though the permeability distribution had sharp contrasts (see third row in Fig. 11), the resulting pressure field was very smooth. For Case E4, permeability heterogeneity was observed to have no influence in altering the frequency-magnitude behavior compared to the homogeneous fault for the model parameters used in this study. The homogeneous fault had a hydraulic aperture of $e_0 = 0.0003$ m, corresponding to a permeability of $k^f = e^2/12 = 7500$ d (darcies). In the heterogeneous models, the hydraulic aperture perturbation at one standard deviation was $\delta e = 0.1 e_0$.

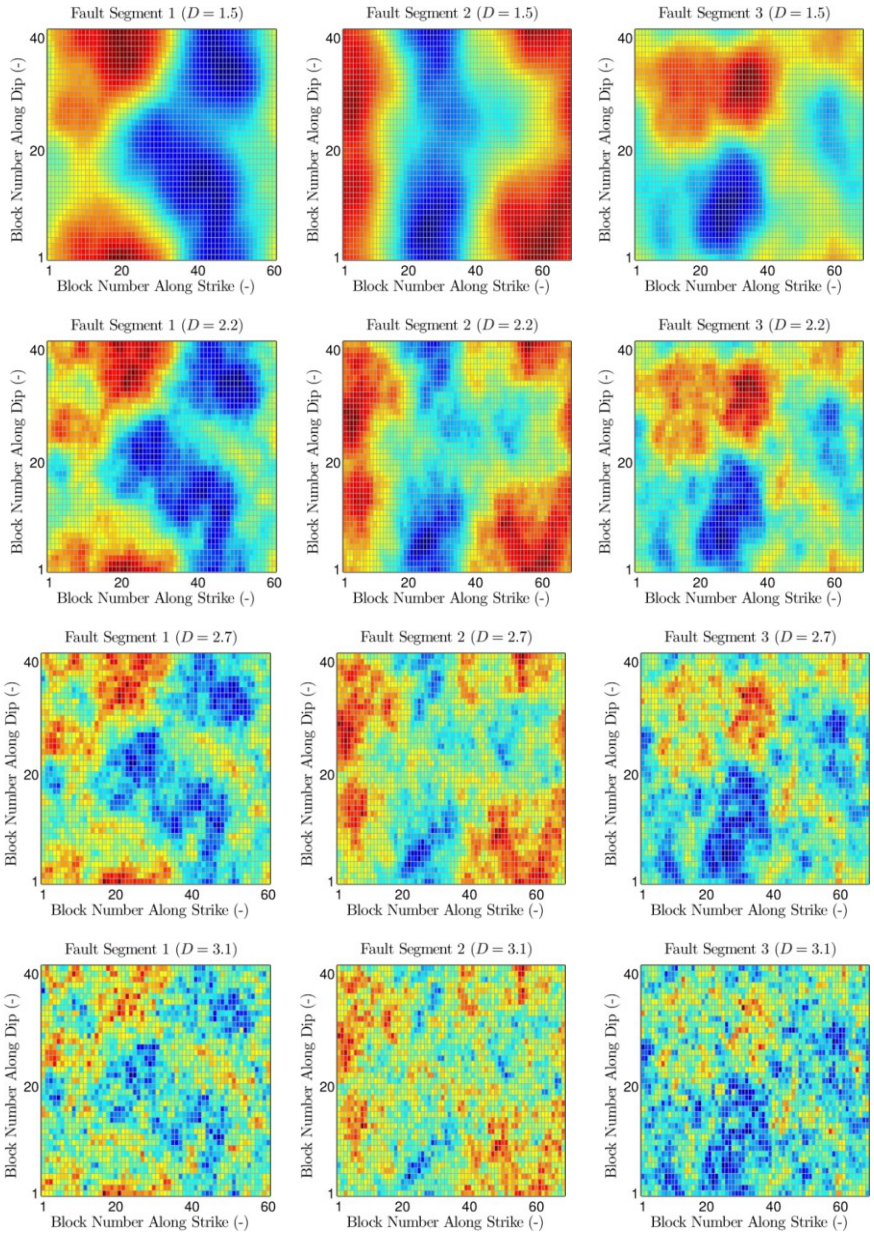

Figure 11: Heterogeneity patterns across each en-echelon fault segment in the numerical model.

4.3.2 Case F: Low Stress Drop

We were motivated to investigate the influence of stress drop on the frequency-magnitude distributions of injection-induced earthquakes because of a phenomenon called pressure-constrained rupture arrest. Dieterich (2015) and Gischig (2015) performed quasidynamic earthquake rupture simulations on two-dimensional and one-dimensional faults, respectively. Both investigations showed that earthquake ruptures could be confined entirely within regions of the fault that experienced significant pressure changes. However, they

also observed that if the background shear stress was raised high enough, the ruptures would tend to propagate across the entire fault. This behavior can be interpreted from the perspective of a rupture dynamics earthquake energy balance. The rupture and arrest processes are governed by a competition between fracture energy and energy release rate (Eshelby, 1969). In the limit that fracture surface energy tends to zero, then a positive energy release rate will cause instability leading to earthquake rupture. The energy release rate scales with the stress intensity factor at the rupture tip, which in turn depends on the stress drop behind the rupture front. Consider a region of the fault subjected to a pressure change, Δp^f . The stress drop is:

$$\Delta \tau = \tau^R - f_D \bar{\sigma}_n^R + f_D \Delta p^f \ . \tag{32}$$

The shear and normal stress resolved on the fault depend on the stress state and fault orientation, and the dynamic friction coefficient depends on rate-and-state friction properties. Therefore, there is no constraint on the value of $\left(\tau^R - f_D \bar{\sigma}_n^R\right)$. If $\left(\tau^R - f_D \bar{\sigma}_n^R\right) < 0$, then a stress drop can only occur over the pressurized region and earthquake ruptures will tend to be confined to that zone. On the other hand, if $\left(\tau^R - f_D \bar{\sigma}_n^R\right) > 0$, the main effect of the pressure perturbation is to help nucleate the event. Upon nucleation, the rupture will tend to propagate until it reaches the fault boundary.

In Case F we assigned a higher value of f_D to the fault than in Case E in an attempt to promote pressure-constrained rupture behavior. We hypothesized that pressure-constrained behavior would tend to produce a larger number of relatively smaller events (i.e., increase the GR b-value) and generate a broader range of event magnitudes as the pressure perturbation gradually spread across the fault.

In Cases F1-F3, the power law scaling was indeed defined over a larger range of magnitudes compared to Case E. For Cases F1 and F2, the GR b-value slightly larger than 1 was stable over a range of $1.5 < M < 3.0$. Different values of D did not have a large influence. For Case F3, a very consistent GR b-value of 1 was observed over the range of $1.5 < M < 4.0$ for each value of D . Similar to Case E4, permeability heterogeneity in Case F4 had no influence on the frequency-magnitude distribution.

5. CONCLUDING REMARKS

We implemented several new physical processes into an existing reservoir simulator to improve the model's ability to simulate injection induced seismicity. In the model, fluid flow and heat transfer calculations are performed using an embedded fracture approach. Poroelastic and thermal stresses are calculated using a finite element method, resolved onto fracture surfaces, and introduced as additional traction boundary conditions in the fracture deformation calculations. The rate-and-state friction component was upgraded to enable quasidynamic earthquake rupture calculations on two-dimensional heterogeneous fault surfaces. A spatial random field model was applied to generate heterogeneous spatially correlated distributions of fault properties.

In collaboration with other members of the DOE code comparison project, we developed a conceptual model of the Fenton Hill Phase II reservoir and performed simulations of several hydraulic stimulation treatments. Our simulation results demonstrate that a mixed-mechanism process where stimulation occurs through mechanical opening of natural fractures and propagation of hydraulic splay fractures is consistent with most of the observations from the field experiments. We investigated the relative influence of fracture pressurization, poroelastic stress, and thermal stress during injection. An important result was that even though the magnitudes of the poroelastic and thermal stresses were much smaller than the pressure changes in the fractures, they had a significant impact on the seismicity rate and overall migration of the microseismic cloud. In the Fenton Hill microseismic catalog data, post shut-in events tended to occur at the edges of the stimulated region. The results from our simulations suggest that thermal effects likely contributed to this behavior.

For application to wastewater disposal settings, we are interested in understanding how the GR b-value can be influenced by injection operations. As a first step, we performed a study to learn how fault heterogeneity affects the frequency-magnitude distribution of simulated earthquake events using a quasidynamic rate-and-state friction model. We investigated heterogeneity in initial shear stress, initial normal stress, dynamic friction coefficient, and permeability. In each case, the model generated hundreds to thousands of individual earthquake events over a 10 year injection duration, so the GR b-value was able to be characterized. For the base case scenarios with homogeneous fault properties, the earthquake sequences did not display GR-type behavior and tended to be dominated by a small number of large events. For the cases of heterogeneous stress and friction, GR b-values slightly above 1 were observed. The GR b-values were observed to vary modestly when the range of spatial correlation was changed. For example, when normal stress was heterogeneous, the GR b-value varied from 1.0 to 1.3 as the range of spatial correlation increased. The state of stress, fault properties, and flow regimes conducive to creating pressure-constrained rupture behavior produced steeper GR b-values. The results suggest a possible relationship between the GR b-value, geologic conditions, and injection operations.

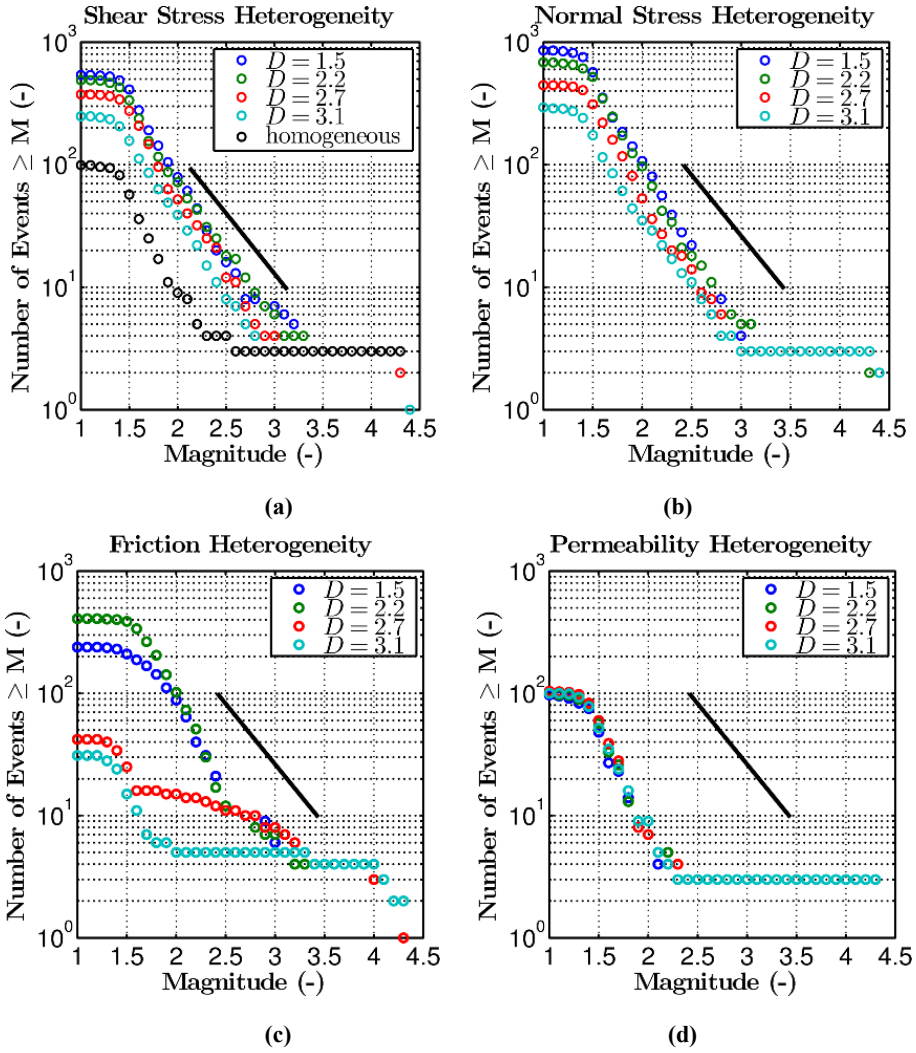

Figure 12: Simulated frequency-magnitude distributions for the large stress drop case (Case E). The solid black line represents a GR b-value of one.

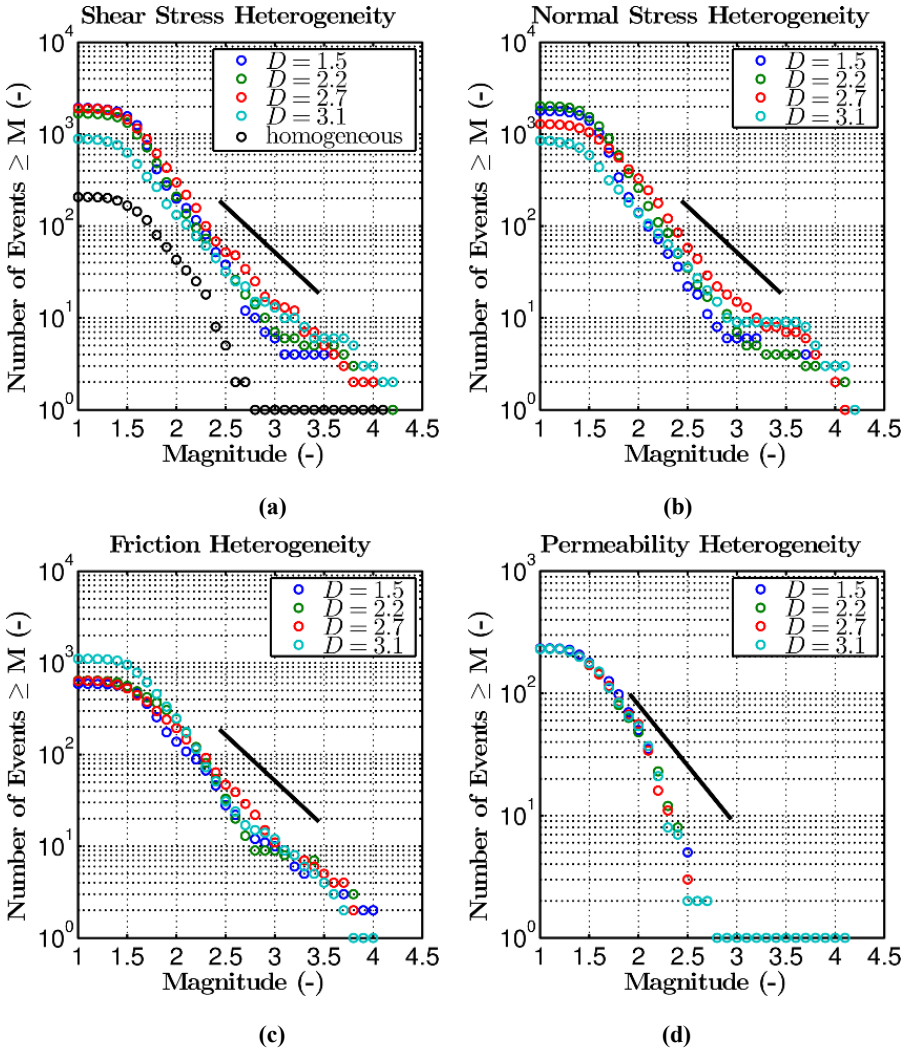

Figure 13: Simulated frequency-magnitude distributions for the low stress drop case (Case F). The solid black line represents a GR b-value of one.

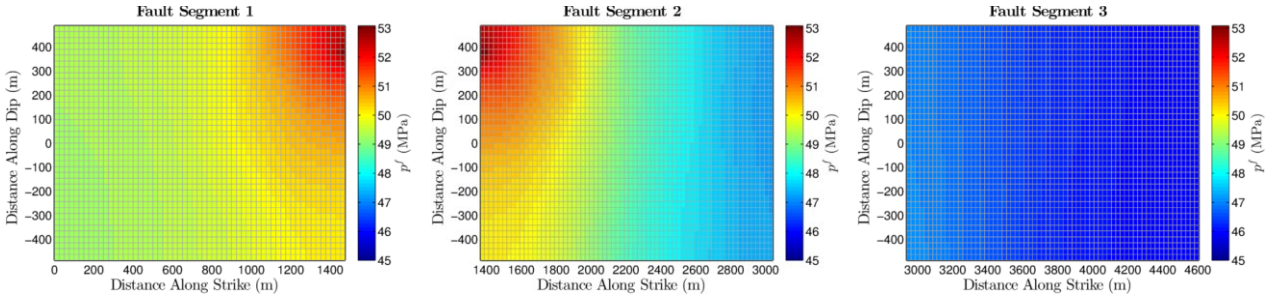

Figure 14: Pressure distribution along fault for Case E4 (fractal dimension 2.7) after 422 days of injection.

ACKNOWLEDGEMENTS

Part of this work was supported by the Department of Energy Geothermal Technologies Office geothermal code comparison study under grant number DE-EE0006646. The financial support of the industrial affiliates at the Stanford Center for Induced and Triggered Seismicity is gratefully acknowledged.

NOMENCLATURE

Roman Variables

Variable	Description	Variable	Description
a	Direct effect parameter in rate-and-state friction model	$\mathbf{k}$	Finite element stiffness matrix
b	State evolution parameter in rate-and-state friction model	K	Drained bulk modulus
$\mathbf{B}$	Finite element strain-displacement matrix	L	Characteristic slip-weakening distance in rate-and-state friction model (or length of a fault patch when subscripted)
c	Specific heat capacity	$\tilde{m}$	Mass source normalized by reference bulk volume
D	Fractal dimension (or hydraulic diffusivity in Figs. 3 and 6)	M	Earthquake event magnitude
$\mathbf{D}$	Finite element stress-strain matrix	κ	Spatial wave number
e	Hydraulic aperture	S	Fracture (fault) cohesion
E	Void aperture	t	Time
f	Coefficient of friction	T	Temperature
$\mathbf{f}$	Body force vector	$\mathbf{u}$	Rock displacement vector
G	Shear modulus	$\mathbf{v}$	Fluid velocity vector
$\mathbf{I}$	Identity matrix	V	Sliding velocity
k	Permeability	W	Physical width (i.e., aperture) of a fracture or fault

Greek Variables

Variable	Description	Variable	Description
α	Biot's coefficient	λ	Inverse fluid viscosity
β	Linear thermal expansion coefficient	Λ	Lame's modulus
δ	Displacement discontinuity	$\tilde{\Pi}$	Matrix-fracture heat transfer normalized by bulk volume or bulk surface area
δb	Perturbation to rate-and-state b parameter	ρ	Fluid density
δe	Perturbation to hydraulic aperture	σ	Stress
$\delta\bar{\sigma}$	Perturbation to normal stress	$\bar{\sigma}$	Effective stress
$\delta\tau$	Perturbation to shear stress	$\boldsymbol{\sigma}$	Stress tensor
ε	Strain	τ	Shear stress acting on the fault

$\boldsymbol{\varepsilon}$	Strain tensor	$\bar{\tau}$	Frictional resistance to shear failure, i.e., shear strength
η	Radiation damping parameter	$\Delta\tau$	Shear stress drop during an earthquake
θ	Fracture (fault) orientation	ϕ	Porosity
Θ	State variable in rate-and-state friction model	$\tilde{\Psi}$	Matrix-fracture mass transfer normalized by bulk volume or bulk surface area
κ	Thermal conductivity	ω	Geometric transmissibility for matrix-fracture heat transfer
κ	Spatial wave number		

Subscript Notation

Subscript	Description	Subscript	Description
C	Coulomb stress	0	Reference state
D	Dynamic or residual	$*$	Reference value in the steady-state friction model
max	maximum	h, H, V	Orthogonal coordinate system where the horizontal and vertical stresses are the principal stresses
r	Rock	x, y, z	Orthogonal Cartesian coordinate system
ss	Steady-state	n, s, d	Orthogonal coordinate system centered on a fracture plane indicating normal, strike, and dip directions, respectively
φ	Fluid		

Superscript Notation

Superscript	Description	Superscript	Description
f	Fracture domain	R	Remote (tectonic)
m	Matrix domain	T	Thermoelastic effect
M	Mechanical effect due to fracture deformation	w	Well domain
P	Poroelastic effect		

REFERENCES

Andrews, D.J.: A stochastic fault model, I, Static case, *Journal of Geophysical Research*, **85**, (1980), 3867-3877.

Barton, C.A., and Zoback, M.D.: In-situ stress orientation and magnitude at the Fenton geothermal site, New Mexico, determined from wellbore breakouts, *Geophysical Research Letters*, **15**(5), (1988), 467-470.

Bradley, A.M.: Software for efficient static dislocation – Traction calculations in fault simulators, *Seismological Research Letters*, **85**(6), (2014).

Brown, D. W.: The potential for large errors in the inferred minimum earth stress when using incomplete hydraulic fracturing results, *International Journal of Rock Mechanics and Mining Sciences & Geomechanics Abstracts*, **26**(6), (1989), 573-577.

Brown, D.W., Duchane, D.V., Heiken, G., and Hriscu, V.T.: *Mining the Earth's Heat: Hot Dry Rock Geothermal Energy*, Springer, (2012).

Dieterich, J.H., Richards-Dinger, K.B., and Kroll, K.A.: Modeling injection-induced seismicity with the physics-based earthquake simulator RSQSim, Seismological Research Letters, 86(4), (2015), 1-8.

Dunham, E.M., Belanger, D., Cong, L., and Kozdon, J.E.: Earthquake ruptures with strongly rate-weakening friction and off-fault plasticity, 1: Planar faults, *Bulletin of the Seismological Society of America*, **101**(5), (2011), 2308-2322.

Fang, Z., and Dunham, E.M.: Additional shear resistance from fault roughness and stress levels on geometrically complex faults, *Journal of Geophysical Research: Solid Earth*, **118**, (2013), 3642-3654.

Eshelby, J.D.: The elastic field of a crack extending non-uniformly under general anti-plane loading, Journal of Physical Solids, 17, (1969), 177-199.

Gischig, V.S.: Rupture propagation behavior and the largest possible earthquake induced by fluid injection into deep reservoirs, *Geophysical Research Letters*, **42**, (2015), 7420-7428.

Horne, R.N.: *Modern Well Test Analysis: A Computer-Aided Approach*, 2nd edn. Petroway Inc., Palo Alto (1995).

House, L., Keppler, H., and Kaieda, H.: Seismic studies of a massive hydraulic fracturing experiment, *Transactions*, Geothermal Resources Council, **9**(2), (1985), 105-110.

Ishibashi, T., Watanabe, N., Hirano, N., Okamoto, A., and Tsuchiya, N.: Beyond-laboratory-scale prediction for channeling flows through subsurface rock fractures with heterogeneous aperture distributions revealed by laboratory evaluation, *Journal of Geophysical Research: Solid Earth*, **120**, (2015), 106-124.

Jaeger, J.C., Cook, N.G.W., and Zimmerman, R.: *Fundamentals of Rock Mechanics*, 4th ed. Blackwell Publishing Ltd., Oxford, (2007).

Kelkar, S., Murphy, H., and Dash, Z.: Earth stress measurements in deep granitic rock, *Proceedings*, The 27th U.S. Symposium on Rock Mechanics, Tuscaloosa, Alabama, USA, 23-25 June (1986).

Mai, P.M., and Beroza, G.C.: A spatial random field model to characterize complexity in earthquake slip, *Journal of Geophysical Research,* **107**(B11), (2002), 2308.

McClure, M.W., Babazadeh, M., Shiozawa, S., and Huang, J.: Fully coupled hydromechanical simulation of hydraulic fracturing in 3D discrete-fracture networks, *SPE Journal*, (2016), published online 1 January 2016.

McClure, M.W., and Horne, R.N.: Investigation of injection-induced seismicity using a coupled fluid flow and rate/state friction model, *Geophysics*, **76**(6), (2011) 181-198.

McClure, M. W.: Modeling and characterization of hydraulic stimulation and induced seismicity in geothermal and shale gas reservoirs, PhD dissertation, Stanford University, Stanford, California, (2012).

McClure, M.W., and Horne, R.N.: *Discrete Fracture Network Modeling of Hydraulic Stimulation: Coupling Flow and Geomechanics*, SpringerBriefs in Earth Sciences, Springer (2013).

McClure, M. W., and Horne, R.N.: An investigation of stimulation mechanism in Enhanced Geothermal Systems, *International Journal for Rock Mechanics and Mining Sciences*, **72**, (2014), 242-260.

Nelson, P.H., Gianoutsos, N.J., and Drake III, R.M.: Underpressure in Mesozoic and Paleozoic rock units in the Midcontinent of the United States, AAPG Bulletin, 99(1), (2015), 1861-1892.

Noda, H., Dunham, E., and Rice, J.R.: Earthquake ruptures with thermal weakening and the operation of major faults at low overall stress levels, *Journal of Geophysical Research*, **114**, (2009), B07302.

Norbeck, J.H., and Horne, R.N.: Physical mechanisms related to microseismic-depletion-delineation field tests with application to reservoir surveillance. *SPE Journal*, (2016), published online 1 January 2016.

Norbeck, J.H., and Horne, R.N.: Injection-triggered seismicity: an investigation of porothermoelastic effects using a rate-and-state earthquake model, *Proceedings,* Fourtieth Workshop on Geothermal Reservoir Engineering, Stanford, California, USA, 26-28 January (2015).

Norbeck, J.H., McClure, M.W., Lo, J.W., and Horne, R.N.: An embedded fracture modeling framework for simulation of hydraulic fracturing and shear stimulation. *Computational Geosciences*, (2015), published online 13 November 2015.

Okubo, P.G., and Aki, K.: Fractal geometry in the San Andreas Fault system, *Journal of Geophysical Research*, **92**, (1987), 345-355.

Petersen, M.D., Moschetti, M.P., Powers, P.M., et al.: The 2014 United States National Seismic Hazard Model, *Earthquake Spectra*, **31**(S1) (2015), S1-S30.

Rice, J.R., Lapusta, N., and Ranjith, K.: Rate and state dependent friction and the stability of sliding between elastically deformable solids, *Journal of the Mechanics and Physics of Solids*, **49**, (2001), 1865-1898.

Rojas, O., Dunham, E.M., Day, S.M., Dalguer, L.A., and Castillo, J.E.: Finite difference modelling of rupture propagation with strong velocity-weakening friction, *Geophysical Journal International*, **179**(3), (2009), 1831-1858.

Smith, I.M., Griffiths, D.V., and Margetts, L.: *Programming the Finite Element Method*, 5th edn. John Wiley and Sons Ltd., (2014).

van der Elst, N., Induced earthquakes are as large as (statistically) expected, *Abstracts*, AGU Fall Meeting, San Francisco, California, USA (2015).

Voss, R.F.: Fractals in nature: From characterization to simulation, in *The Science of Fractal Images*, edited by H.-O Peitgen and D. Saupe, 21-70, Springer-Verlag, New York (1988).

Weng, X., Kresse, O., Cohen, C.-E., Wu, R., and Gu, H.: Modeling of hydraulic-fracture-network propagation in a naturally fractured formation, *SPE Production & Operations*, **26**(4), (2011).

White, S.K., Purohit, S., and Boyd, L.: Using GTO-Velo to facilitate communication and sharing of simulation results in support of the Geothermal Technologies Office code comparison study, *Proceedings,* Fourtieth Workshop on Geothermal Reservoir Engineering, Stanford, California, USA, 26-28 January (2015).

APPENDIX A: RESERVOIR MODEL PROPERTIES

Table A-1: Model parameters for Fenton Hill seismicity study in Section 3.

Parameter	Value	Unit	Parameter	Value	Unit
c_φ	4200	kJ/(kg · °C)	α	0.4	-
c_r	800	kJ/(kg · °C)	β	8×10^{-6}	1/°C
$\rho_{\varphi 0}$	1000	kg/m^3	p_0	31	MPa
ρ_r	2650	kg/m^3	T_0	230	°C
k^m	1×10^{-19}	m^2	T^w	130	°C
ϕ^m	0.05	-	f	0.7	-
e_0	0.0004	m	S	0.5	MPa
E_0	0.0004	m	G	15	GPa
κ_φ	0.6	W/(m · °C)	Λ	15	GPa
κ_r	2.4	W/(m · °C)	σ_H^R	90	MPa
λ^{-1}	0.00015	Pa · s	σ_h^R	46	MPa

Table A-2: Model parameters for GR b-value study in Section 4.

Parameter	Value	Unit	Parameter	Value	Unit
a	0.01	-	E_0	0.001	m
b (Case E)	0.014	-	λ^{-1}	0.0008	Pa · s
b (Case F)	0.012	-	$\rho_{\varphi 0}$	930	kg/m^3
L	0.005	m	p_0	45	MPa
f_*	0.6	-	σ_H^R	145	MPa
V_*	1×10^{-10}	m/s	σ_h^R	75	MPa
G	15	GPa	θ_s	N60°E	Deg.
Λ	15	GPa	m^w	9.075 (150,000)	kg/s (bbl/month equiv.)
e_0	0.0003	m			